FULL PAPER

# Perturbed spiral real-time phase-contrast MR with compressive sensing reconstruction for assessment of flow in children

**Grzegorz Tomasz Kowalik**[1] (iD)    |    **Daniel Knight**[1,2]    |    **Jennifer Anne Steeden**[1] (iD)    |
**Vivek Muthurangu**[1,3]

[1]Centre for Cardiovascular Imaging, University College London Institute of Cardiovascular Science, London, United Kingdom

[2]Department of Cardiology, Royal Free London NHS Foundation Trust, London, United Kingdom

[3]Great Ormond Street Hospital for Children, London, United Kingdom

**Correspondence**
Grzegorz Tomasz Kowalik, Centre for Cardiovascular Imaging, University College London Institute of Cardiovascular Science, Great Ormond Street Hospital for Children, Great Ormond Street, London, WC1N 3JH, United Kingdom.
Email: grzegorz.kowalik.09@ucl.ac.uk

**Purpose:** we implemented a golden-angle spiral phase contrast sequence. A commonly used uniform density spiral and a new 'perturbed' spiral that produces more incoherent aliases were assessed. The aim was to ascertain whether greater incoherence enabled more accurate Compressive Sensing reconstruction and superior measurement of flow and velocity.

**Methods:** A range of 'perturbed' spiral trajectories based on a uniform spiral trajectory were formulated. The trajectory that produced the most noise-like aliases was selected for further testing. For in-silico and in-vivo experiments, data was reconstructed using total Variation L1 regularisation in the spatial and temporal domains. In-silico, the reconstruction accuracy of the 'perturbed' golden spiral was compared to uniform density golden-angle spiral. For the in-vivo experiment, stroke volume and peak mean velocity were measured in 20 children using 'perturbed' and uniform density golden-angle spiral sequences. These were compared to a reference standard gated Cartesian sequence.

**Results:** In-silico, the perturbed spiral acquisition produced more accurate reconstructions with less temporal blurring (NRMSE ranging from 0.03 to 0.05) than the uniform density acquisition (NRMSE ranging from 0.06 to 0.12). This translated in more accurate results in-vivo with no significant bias in the peak mean velocity (bias: −0.1, limits: −4.4 to 4.1 cm/s; $P = 0.98$) or stroke volume (bias: −1.8, limits: −9.4 to 5.8 ml, $P = 0.19$).

**Conclusion:** We showed that a 'perturbed' golden-angle spiral approach is better suited to Compressive Sensing reconstruction due to more incoherent aliases. This enabled accurate real-time measurement of flow and peak velocity in children.

**KEYWORDS**
compressive sensing, PCMR, real-time

# 1 | INTRODUCTION

Phase-contrast magnetic resonance (PCMR) is a proven method of measuring blood flow in the clinical environment.[1,2] Such acquisitions are usually cardiac-gated, enabling collection of high spatio-temporal resolution data. In children, cardiac gating is often combined with signal averaging to allow free-breathing acquisition with minimal respiratory artifact. However, this is a time-consuming approach that significantly prolongs scan time. Accelerated breath-hold PCMR is an alternative,[3] but some children find even short breath-holds difficult. Thus, a rapid free-breathing approach is desirable.

One solution is real-time imaging and several real-time PCMR sequences have been described.[4] Most rely on a combination of parallel imaging (i.e., SENSE[5] or GRAPPA[6]), efficient k-space filling (i.e., spiral[7] or EPI[8]) and temporal undersampling (i.e., UNFOLD[9] or k-t BLAST[4]) to reduce acquisition time. Unfortunately, these methods fail at very high acceleration rates, limiting the achievable spatio-temporal resolution.

It has been shown that compressive sensing (CS) can reconstruct high quality images from heavily undersampled k-space data.[10] However, a prerequisite of CS is that aliasing is incoherent. One way this can be achieved is by combining non-Cartesian trajectories (i.e., radial[11] or spiral[12]) with golden-angle rotations. Spiral trajectories are of particular interest for PCMR due to short TEs and highly efficient filling of k-space. Golden-angle spiral imaging with CS reconstruction has been shown to be sufficient for real-time cine data.[11,12] However, we have shown in a pilot study[13] that CS reconstruction can cause temporal blurring of PCMR data that could result in underestimation of clinically important metrics. A possible solution may be modification of k-space sampling to produce more incoherent aliases, which should improve data conditioning for the CS reconstruction.

The general aim of this study was to implement a perturbed spiral PCMR acquisition. The specific aims were to (1) find the optimum perturbed spiral trajectories for CS reconstruction of PCMR data using point spread functions (PSFs) and in silico simulations, and (2) validate the developed technique in vivo.

# 2 | METHODS

## 2.1 | Perturbed spiral design

All trajectories were designed using a modification of the method described by Pipe.[14] The starting point for the new trajectory design was a uniform density spiral sequence with 36 evenly spaced interleaves required to completely fill k-space. To perform 1-sided velocity encoding, each readout was acquired twice (velocity encoding and compensation acquisitions). The initial reference trajectory parameters were set to FOV = $450 \times 450$ mm, voxels = $1.76 \times 1.76 \times 6.0$ mm, TR/TE = 8.54/1.93 ms, and velocity encoding = 200 cm/s. These uniform density readouts were continuously rotated by the golden angle (~222°), resulting in a golden-angle spiral acquisition ($GAS_{uniform}$, Figure 1). To achieve the desired temporal resolution (< 30 ms), the $GAS_{uniform}$ sequence was 18-times undersampled (2 interleaves per frame).

Spiral aliases are observed as concentric rings[15,16] in their PSFs (Figure 2), and the position of these aliases depends on the radial undersampling of the spiral trajectory. Thus, it is possible to increase the incoherence of these aliases by modifying the radial undersampling. To achieve this, we developed a trajectory design algorithm that sinusoidally varied the radial acceleration ($\alpha_r$) as a function of normalized distance from k-space center ($r$). This can be described formulaically as follows (and graphically in Supporting Information Figure S1):

$$
\alpha_r = \begin{cases} \dfrac{R + (R-1)\sin(\beta\pi r + \phi_0)}{2} : \beta > 0 \\ 0.5R : \beta = 0 \end{cases}
$$

$$
R = \begin{cases} 1 : r < c_0 \\ \alpha_0 : r \geq c_1 \\ 1 + (\alpha_0 - 1)\dfrac{r - c_0}{c_1 - c_0} : r \geq c_0 \cap r < c_1 \end{cases} \tag{1}
$$

where $\alpha_0$ is the maximum prescribed radial acceleration, $\beta$ is the number of oscillations in $\alpha_r \in [0.5, \alpha_0 - 0.5]$ between the center and edge of k-space, and $\phi_0$ is an additional phase offset. The parameters $c_0$ and $c_1$ ($c_0, c_1$ [0, 1] $\cap c_0 \leq c_1$) divide k-space into 3 sections: (1) a central section ($r < c_0$) with 2-times oversampling ($\alpha_r = 0.5$) and no oscillations; (2) a transition section ($r \geq c_0 \cap r < c_1$) with linearly increasing radial acceleration and oscillation amplitude; and (3) an outer section ($r \geq c_1$) with the maximum acceleration and oscillation amplitude ($\alpha_r = 0.5\alpha_0$ for $\beta = 0$ or $\alpha_r = \alpha_0 - 0.5$ for $\beta > 0$). In this study, $\phi_0$ was varied between 0° and 360° with 10° increments. This produced a set of 36 perturbed trajectories for any given set of $\alpha_0$, $c_0$, $c_1$, and $\beta$ with indices ($j$) between 0 and 35. The exact perturbed trajectory used for any given readout (with an index [$i$] between 0 and infinity) was chosen using the following series index translation:

$$
j = MOD(i, 18) + MOD(i, 2) * 18. \tag{2}
$$

As with $GAS_{uniform}$, consecutive readouts were rotated by the golden angle, resulting in a perturbed golden-angle spiral ($GAS_{perturbed}$) sequence. It should be noted that even though perturbed trajectories were reused (every 36 readouts), they were always in different k-space position due to the golden-angle rotation. Varying the values of $\alpha_0$, $c_0$, $c_1$, and $\beta$ allows different perturbations to be designed, and 2 examples of perturbed spirals trajectories are shown in Figure 1
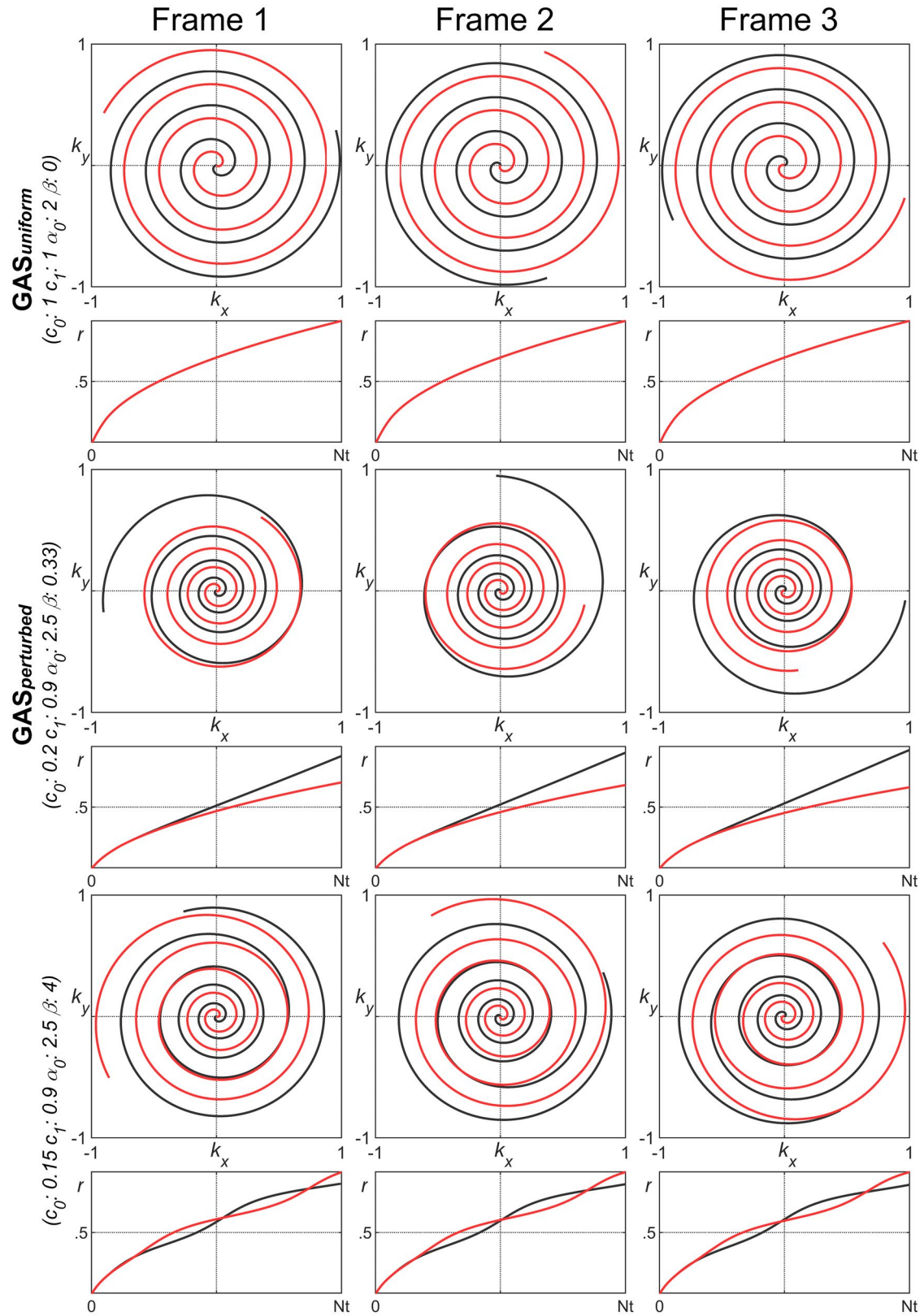
**FIGURE 1** Trajectory visualization. Shown are the uniform golden-angle spiral acquisition (GAS$_{uniform}$), perturbed golden-angle spiral acquisition (GAS$_{perturbed}$), and an additional example presenting possible perturbations induced to the spiral trajectory. The $k_x$-$k_y$ positions of composite trajectories are presented for 3 consecutive imaging frames. Also plotted are variations in the radial distance (r) of individual samples with their coordinates ($k_x$ and $k_y$)
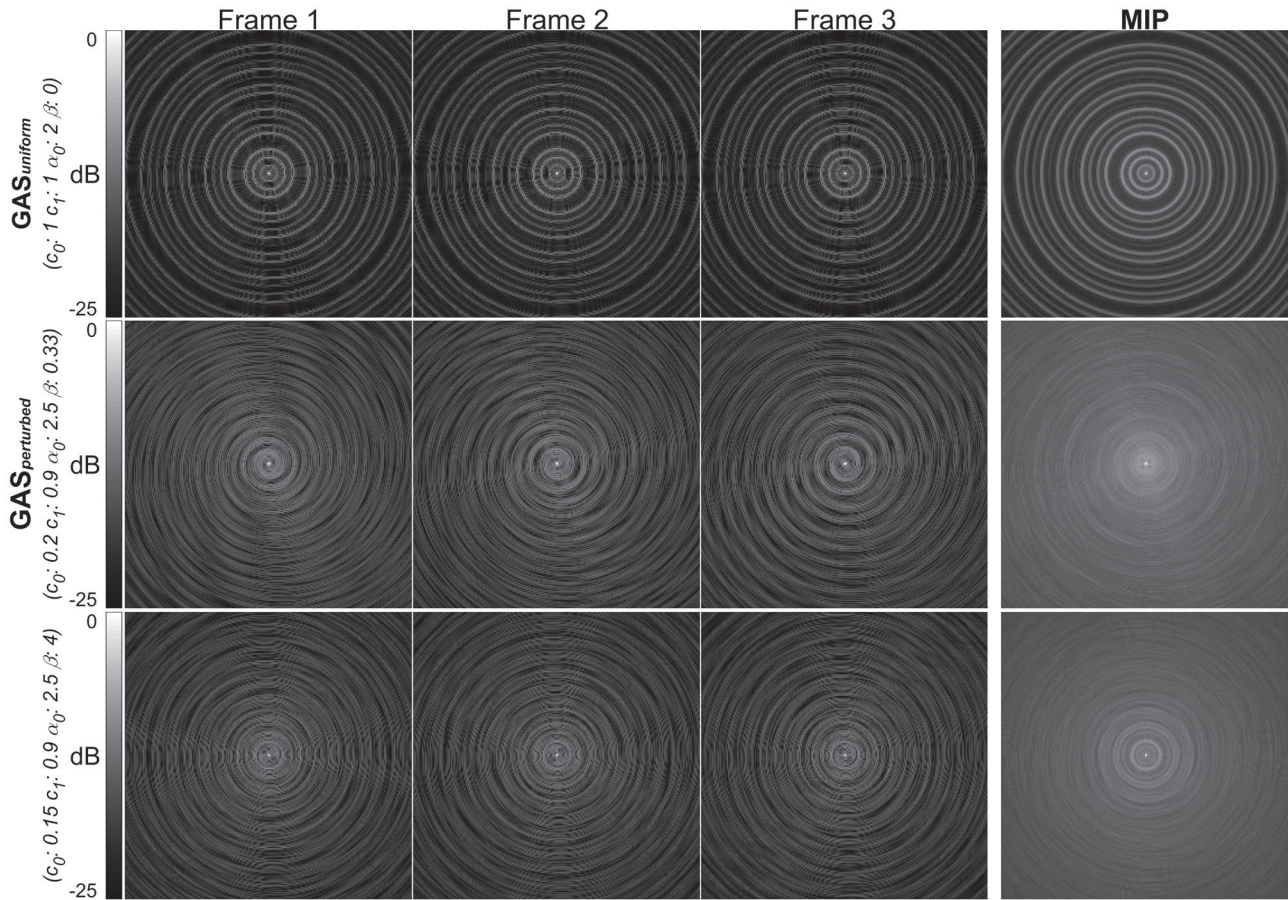
**FIGURE 2** Comparison of point spread functions (PSFs). Presented are the PSFs of $GAS_{uniform}$, $GAS_{perturbed}$, and the example trajectory from Figure 1 for 3 consecutive imaging frames. Additionally, the magnitude intensity projection (MIP) through time (90 consecutive frames) is shown. Multiple of rings that do not change their spatial location can be observed in the PSFs of $GAS_{uniform}$. These rings are clearly visible in the MIP image. The broader spatial distribution of the aliasing rings can be observed on all of the PSFs for the other trajectories; however, the selected $GAS_{perturbed}$ trajectory is better in dispersing these patterns temporally, which resulted in a more uniform MIP image. The PSFs were prepared for a FOV of 450 mm and normalized to the central point. All PSFs have the same logarithmic color scale

(see Supporting Information Figure S2 for accompanying $k_x$ and $k_y$ versus time plots).

One issue with perturbed spirals is that the number of readout samples required to reach the edge of k-space may vary. Consequently, we restricted the number of readout samples to the number in the shortest readout for a given set of parameters ($\alpha_0$, $c_0$, $c_1$, and $\beta$). This was done to ensure a constant TR throughout the acquisition and resulted in some readouts terminating before reaching k-space edge (Figure 1). The $GAS_{perturbed}$ can also have different sampling acceleration ($SA = N_i/N_t$, in which $N_i$ represents the image pixels and $N_t$ the total trajectory samples) when compared with $GAS_{uniform}$. Therefore, the number of readouts combined into an imaging frame had to be adjusted for each set of parameters, to ensure comparable acquisition times and $SA$. This was incorporated into test scripts using the $GAS_{uniform}$ trajectory as a reference point ($N_t^{uniform} = 5862$, $SA^{uniform} = \sim 11.2$). Due to the impact of multiple excitation times and inability to split readout samples, the maximum

number of readouts was set to 3 and the minimum sampling acceleration to 93% of $SA^{uniform}$.

## 2.2 | Point spread function evaluation

The $GAS_{petrubed}$ should produce more incoherent aliases than $GAS_{uniform}$. However, the level of incoherency will depend on $\alpha_0$, $c_0$, $c_1$, and $\beta$, which must be optimized. The PSF is used commonly to ascertain the features of a given sampling pattern and optimize trajectory parameters. In this study, we used the amount of energy leakage to the PSF side lobes[17] as an incoherence metric ($\times$ point-by-point multiplication):

$$\text{Energy Leakage} = ||PSF_{x,y} \times (x^2 + y^2)^{\frac{1}{4}}||^2. \quad (3)$$

The calculations were done for all combinations of $\alpha_0$, $c_0$, $c_1$, and $\beta$ given in Table 1. The trajectory ($GAS_{perturbed}$, Figure 1) with the lowest average energy leakage (Figure 3,

indicating higher incoherence of artifacts) was selected for further tests.

## 2.3 | Reconstruction

Compressive sensing solves a set of nonlinear equations (representing the imaging process) through minimization of a cost function. The cost function used in this study is

$$\underset{\rho}{argmin} \left\{ ||E\rho - y||_2^2 + \lambda_1 ||TV_t\rho||_1 + \lambda_2 ||TV\rho||_1 \right\}. \quad (4)$$

The first term enforces data consistency, where $\rho$ are the image data, $E$ is the encoding matrix (the multicoil nonuniform Fourier transform operator), and $y$ are the acquired k-space data. The additional terms enforce sparse results through L1 norm regularization. In this study, finite difference operators (or total variation) were applied in space and time ($TV$ [spatial], $TV_t$ [temporal]) as the sparse transforms.

The optimization was performed using a nonlinear conjugate gradient algorithm. For fast reconstruction, the described CS algorithm was implemented on an external

graphics processing unit–equipped computer (Tesla K40c; NVIDIA, Santa Clara, CA) with online communication to the native reconstructor.[18] Acquired data were reconstructed in blocks of 90 frames with coil-sensitivity maps calculated from the time-averaged (flow-compensated) data from each block. These blocks were overlapped by 3 frames on each side to counter potential jump discontinuities. If there was no adjacent block (the start and end of the first and last block), the expansion was achieved by mirroring frames.

Gridding of non-Cartesian samples onto a rectilinear grid[19,20] requires information about the density of the samples. This is not provided by the described trajectory generation algorithm. Consequently, density compensation coefficients were calculated using the method described in Bydder,[21] which was chosen because it required no fine-tuning. The method uses a linear optimization process to find density distributions for a set of arbitrary trajectory points. The sample's density calculation was implemented as the first step of the graphics processing unit–based MRI reconstruction process.

## 2.4 | In silico model

The GAS_uniform and chosen GAS_perturbed sampling patterns were first evaluated in an in silico model, enabling comparison with ground-truth data. The in silico model (Supporting Information Figure S3) consisted of a cross section of the body through the ascending aorta. Aortic velocity, distension, signal intensity, and in-plane motion were modeled on data extracted from a high temporal resolution (~20 ms)

**TABLE 1** Range of the tested trajectory design parameters

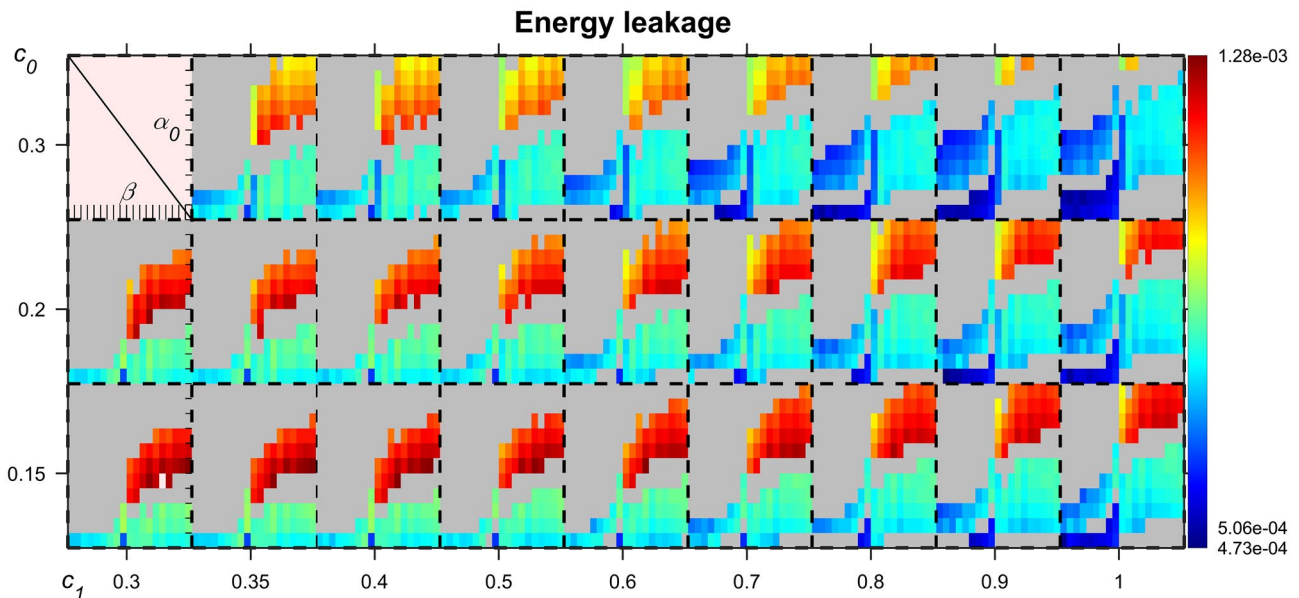| | |
|---|---|
| $c_0$ | 0.15, 0.2, 0.3 |
| $c_1$ | 0.3, 0.35, 0.4, 0.5, 0.6, 0.7, 0.8, 0.9, 1 |
| $\alpha_0$ | 2.5, 3, 3.5, 4, 4.5, 5, 6, 7, 8, 9, 10 |
| $\beta$ | 0.2, 0.25, 0.33, 0.5, 0.66, 0.75, 1, 1.25, 1.5, 2, 3, 4, 5, 6, 7, 8, 9, 10 , 12, 15 |



**FIGURE 3** Energy leakage results for all of the tested trajectory parameters (Table 1). The gray color indicates the parameters that yielded an incompatible trajectory—the maximum number of readouts or the minimum samping acceleration were exceeded. The minimum energy leakage of $4.73^{-4}$ was found for $c_0 = 0.2$ (the middle grid row), $c_1 = 0.9$ (the second grid column from the right), $\alpha_0 = 2.5$, and $\beta = 0.33$ (the third element in the last line of the pointed grid tile)

Cartesian-gated PCMR data set acquired in a healthy volunteer. Respiratory motion was modeled using a function consisting of expansion (inhalation), a brief pause, and contraction (exhalation). The respiratory rate was set to 10 breaths per minute with the maximum body contraction to 98% of its original size.

Simulated MR data were created by generating the image data at each of the readout time positions. The readout time was set to the $GAS_{uniform}$ TR of 8.54 ms. The complex phase component was generated through interpolation of the flow curve. The produced models were scaled with synthetically generated coil sensitivity maps (12 coils as in the in vivo experiment). This was then transformed into k-space and gridded onto the tested trajectory.

The in silico reconstructions were performed with multiple regularization levels ($\lambda_1 \in \{0.25e^{-4}, 0.5e^{-4}, 0.75e^{-4}, 1e^{-4}, 2.5e^{-4}, 2.75e^{-4}, 3e^{-4}, 3.25e^{-4}, 4e^{-4}, 5e^{-4}, 7.5e^{-4}\}$ and $\lambda_2 \in \{0.25e^{-5}, 0.5e^{-5}, 0.75e^{-5}, 1e^{-5}, 5e^{-5}, 7.5e^{-5}, 10e^{-5}, 12.5e^{-5}\}$) to ensure that the reconstruction was optimized for the specific sampling pattern. Reconstructed in silico data were compared against a reference standard generated using a fully sampled uniform density regular angle spiral trajectory and reconstructed with a SENSE algorithm.[5,7,22] The assessment was done comparing differences between individual pixel's phase values extracted from the simulated aortic cross sections using normalized RMS error (NRMSE).

## 2.5 | In vivo study

The $GAS_{uniform}$ and chosen $GAS_{perturbed}$ sampling patterns were also assessed in a patient population consisting of 20 children referred for cardiac clinical MR (7 females and 13 males; age range: 6-16, median: 12.5 years). The only exclusion criterion was irregular rhythm (i.e., multiple ectopic beats or atrial fibrillation). The National Research Ethics Committee approved the study (06/Q0508/124), and written consent was obtained from all patients or legal guardians of children.

All imaging was performed on a 1.5T MR scanner (Magnetom Avanto; Siemens Medical Solutions, Erlangen, Germany) using the standard 2 spine coils and 1 body matrix coil setup (giving a total of 12 coil elements) used in all children at our institution. A vector electrocardiographic system was used for cardiac gating in the reference Cartesian-gated PCMR acquisitions. The imaging plane for aortic flow assessment was located in the ascending aorta just above the sino-tubular junction. The reference standard flow acquisition was a conventional free-breathing Cartesian retrospectively gated PCMR sequence with the following parameters: FOV = 350 × 262 mm, voxels = 1.82 × 1.82 × 6.0 mm, TR/TE = 4.4/1.9 ms, flip angle = 30º, velocity encoding = 200 cm/s, number of signal averages = 2, GRAPPA = 2, and temporal resolution = 18.5 ms.

Both real-time GAS PCMR acquisitions were set to FOV = 450 × 450 mm, voxels = 1.76 × 1.76 × 6.0 mm, flip angle = 20º, and velocity encoding = 200 cm/s. The bandwidth per pixel was optimized separately to minimize the trajectory errors' impact on image quality. This was done empirically based on a single in vivo case. These adjustments affected the length of a readout. The final TR/TE values were 6.7/1.9 ms for the $GAS_{perturbed}$ and 7.5/1.9 ms for $GAS_{uniform}$ acquisitions, resulting in a temporal resolution of approximately 26.6 ms (about 2.4 seconds for 90 frames) and approximately 29.9 ms (about 2.7 seconds for 90 frames), respectively. A relatively large FOV was chosen to ensure that even in older children there was no signal from outside the FOV.

The regularization parameters ($\lambda_1$, $\lambda_2$) were selected empirically as a trade-off between image quality and minimization of spatial and temporal blurring.

## 2.6 | Flow quantification

The aorta was segmented on the magnitude images using a semi-automatic method based on the optical flow registration[23] with manual operator correction using in-house plugins for Osirix software (OsiriX Foundation, Switzerland).[24] The resultant regions of interest (ROIs) were transferred to the phase images to produce flow and velocity curves. Maximum velocity was taken as the peak of the velocity curve. Stroke volume was calculated by integrating the resultant flow curve over a single r-r interval. As multiple heartbeats are evaluated with real-time PCMR, the stroke volume and peak velocity are averaged across all r-r intervals.

## 2.7 | Image quality

All quantitative analyses were carried out using in-house plug-ins for OsiriX software, version 9.0.[24] True quantification of SNR and velocity-to-noise ratio (VNR) in images acquired with non-Cartesian trajectories is nontrivial in the clinical environment due to the uneven distribution of noise.[25,26] Therefore, in this study, estimated SNR and VNR were calculated as previously described.[27] In summary, an ROI was drawn in stationary tissue, and estimated noise was calculated as the average SD of the pixel intensity ($\sigma_s$) or velocity ($\sigma_v$) through time. Final estimates of SNR and VNR were made by dividing the mean signal intensity from an ROI drawn at peak systole by $\sigma_s$ and $\sigma_v$, respectively.

Quantitative edge sharpness was calculated in peak systole by measuring the average maximum gradient of the normalized pixel intensities across the aortic wall. The image data were resampled onto evenly spaced perpendicular lines crossing the vessel border (marked with the ROIs used to extract the velocity data). Lanczos resampling[28,29] was used with a 0.5-mm step between samples on the lines with a

distance of 20 mm. Furthermore, the smooth noise robust differentiation[30] was applied to extract the maximum gradient on the projections.

In real-time data, the SNR, VNR, and edge sharpness measurements were performed in all peak systole frames, and the averaged values were used in comparisons.

Subjective image quality scoring for the $GAS_{uniform}$ and $GAS_{perturbed}$ sequences was done by 2 independent, experienced observers (V.M. and D.K.) who were presented with the magnitude data for each patient in a blinded, randomized manner. The Cartesian data were not included, as they were obvious to the observer, which risked bias. The images were graded on a Likert scale (1 = very poor [major artifacts exist and the images are not clinically useful], 2 = poor [artifacts exist and clinical use is not advised], 3 = average [able to be used clinically], 4 = good [contains minor artifacts that do not affect clinical use], and 5 = excellent [no artifacts]).

## 2.8 | Statistical analysis

All statistical analyses were performed using R software (R Foundation for Statistical Computing, Vienna, Austria) and a *p*-value of less than .05 indicated a significant difference. All of the results are expressed as mean ± SD. Differences among the 3 imaging techniques were assessed using the 1-way repeated-measures analysis of variance. The imaging techniques were treated as the repeated measure factor. Significant results were further investigated with post hoc pairwise comparison using the Tukey method.

Qualitative image scores were compared using 1-way analysis of variance, as previous work has shown that there is a lower chance of type II errors compared with nonparametric tests for Likert scale data.[31] It is therefore more likely to detect differences among the techniques. The scores provided by the observers were treated as individual factor measures.

## 3 | RESULTS

### 3.1 | Trajectory optimization

Energy leakage results for the range of $GAS_{perturbed}$ trajectories (Table 1) are presented in graphical form in Figure 3. The optimal trajectory was found for the following parameters: $c_0 = 0.2, c_1 = 0.9, \alpha_0 = 2.5$, and $\beta = 0.33$. This corresponds to a trajectory that is oversampled at the center with a low frequency oscillation in radial acceleration that slowly increases in amplitude (Figure 1 and Supporting Information Figure S1). Consequently, each trajectory covers a different portion of k-space and contributes unique information. These temporal sampling density distribution changes are visible in the PSFs as changes in distribution of the side lobes between frames (Supporting Information Figure S4 and Supporting Information Video S1). The PSFs of the $GAS_{uniform}$, the

optimized $GAS_{perturbed}$ trajectory, and 1 of the nonoptimized $GAS_{perturbed}$ trajectories are shown in Figure 2 and Supporting Information Video S1. This visually demonstrates the greater incoherence provided by $GAS_{perturbed}$ trajectories compared with $GAS_{uniform}$ and the importance of optimizing the perturbation to increase incoherence.

### 3.2 | In silico model

Magnitude and phase data reconstructed with optimal regularization parameters (the lowest NRMSE) for $GAS_{perturbed}$ (NRMSE = 0.03, $\lambda_1 = 7.5e^{-5}$, $\lambda_2 = 7.5e^{-5}$) and $GAS_{uniform}$ (NRMSE = 0.06, $\lambda_1 = 4.0e^{-4}$, $\lambda_2 = 5.0e^{-6}$) sequences are shown in Figure 4 along with the velocity curves extracted from these data sets. There is significant blurring of the $GAS_{uniform}$ velocity curve compared with the ground truth, resulting in underestimation of the peak velocity. However, there is minimal blurring of the $GAS_{perturbed}$ velocity curve with good agreement of peak velocity.

The effect of regularization parameters on NRMSE for $GAS_{perturbed}$ and $GAS_{uniform}$ is shown in Figure 5. For $GAS_{uniform}$, increasing temporal regularization ($\lambda_1$) reduces NRMSE, whereas increasing spatial regularization ($\lambda_2$) has a small detrimental effect. This pattern can also be appreciated in the extracted velocity curves at different levels of regularization. At low levels of temporal regularization, curves exhibit artifacts due to unresolved coherent aliasing (Figure 5). Increasing temporal regularization removes these artifacts, but results in temporal blurring. Changing spatial regularization has minimal effect on the shape of the velocity curve for $GAS_{uniform}$. For $GAS_{perturbed}$, all NRMSE results are lower compared with $GAS_{uniform}$, with less variation as a function of regularization (Figure 5). The $GAS_{perturbed}$ velocity curves with different regularization levels are very similar, with none exhibiting artifacts due to coherent aliasing. The highest NRMSEs were found with high levels of temporal regularization, which caused temporal blurring. Conversely, the lowest NRMSEs were found with high levels of spatial regularization and low levels of temporal regularization.

### 3.3 | Feasibility

The PCMR data were successfully acquired in all 20 children during free breathing. Reconstruction time for each real-time block of 90 frames from $GAS_{perturbed}$ and $GAS_{uniform}$ was about 52 seconds, and all 270 frames were available for viewing on the scanner in about 160 seconds. The regularization levels were optimized separately for $GAS_{uniform}$ and $GAS_{perturbed}$. The parameters were set to $\lambda_1 = 5.0e^{-5}$ and $\lambda_2 = 1.0e^{-5}$ for both reconstructions based on a visual assessment of results from a single subject. The mean heart rate of the study population was 81 ± 12 (range: 60-108) beats per minute. The reference standard Cartesian free-breathing gated acquisition
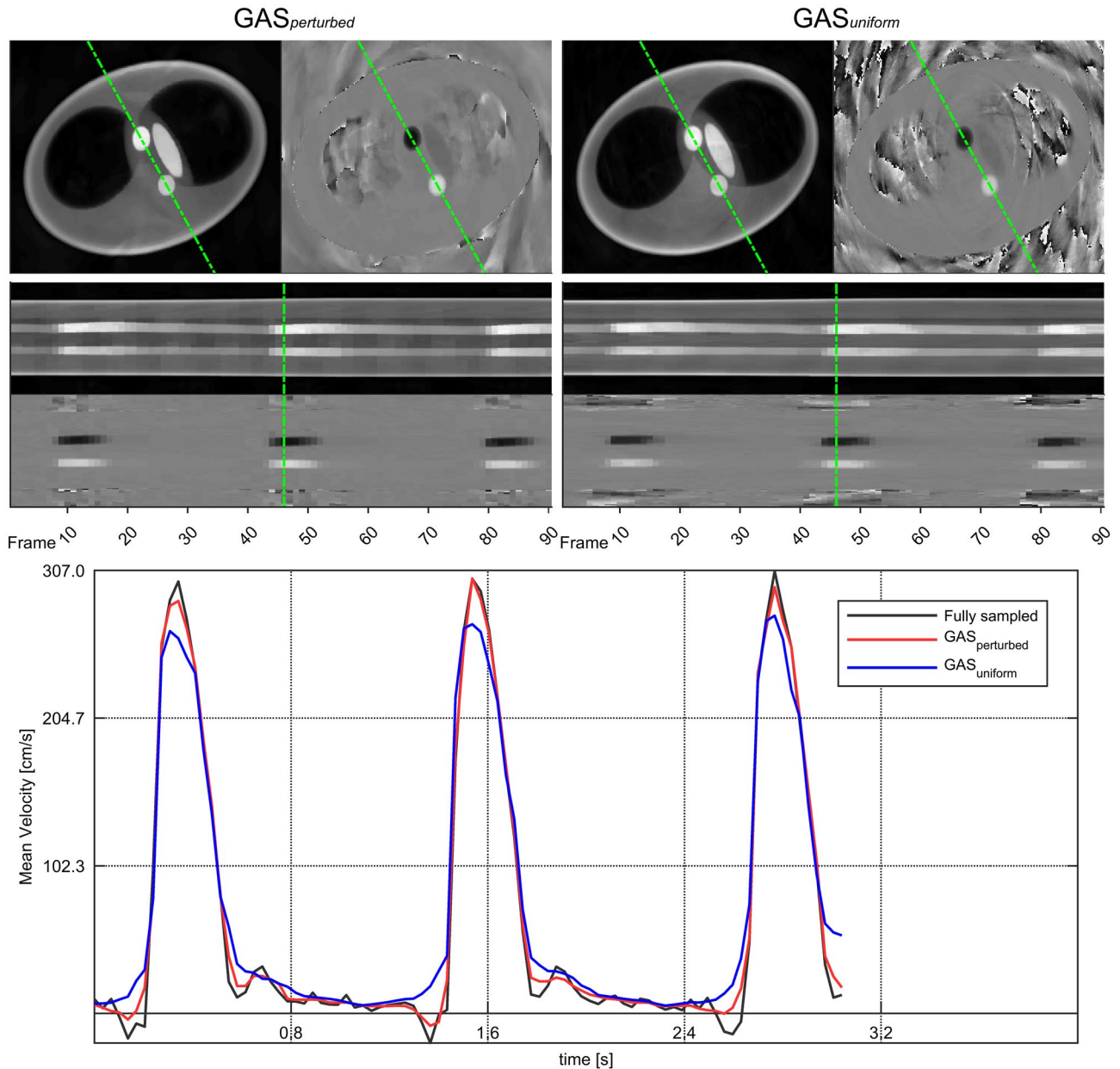
**FIGURE 4** In silico results. The imaging results of the in silico reconstruction present a frame at a peak velocity and a temporal cross section through the simulated ascending and descending aorta, as marked. The bottom plots compare the extracted mean flow aortic velocities for the regularization parameters giving the lowest normalized RMS error (NRMSE)

required 84 heart beats to complete, resulting in $63 \pm 10$ seconds (range: 47-84 seconds) acquisition time.

## 3.4 | In vivo flow quantification

Examples of velocity and flow curves generated by the Cartesian, GAS$_{uniform}$, and GAS$_{perturbed}$ acquisitions from the same subject are shown in Figure 6. As in the in silico results, there is substantial blurring of the velocity curves derived from GAS$_{uniform}$ data. This resulted in significantly lower ($P < .001$) peak velocity measured from the GAS$_{uniform}$ data ($68.7 \pm 18.4$ cm/s) compared with the Cartesian reference

($72.4 \pm 18.0$ cm/s). This bias was also associated with relatively broad limits of agreement (bias: $-3.7$, limits: $-10.4$ to 3.0 cm/s; Figure 7). There was much less blurring of the velocity curve derived from GAS$_{perturbed}$ data ($72.3 \pm 18.6$ cm/s) with no significant difference ($P = .98$) in the peak velocity compared with the Cartesian reference. In addition, there were narrower limits of agreement (bias: $-0.1$, limits: $-4.4$ to 4.1 cm/s; Figure 7).

Aortic stroke volume (Figure 7) results showed no statistical difference between Cartesian ($73.2 \pm 23.7$ mL) and both GAS$_{perturbed}$ ($71.4 \pm 23.4$ mL, $P = .19$) and GAS$_{uniform}$ ($74.5 \pm 26.0$ mL, $P = .40$) acquisitions. The GAS$_{perturbed}$
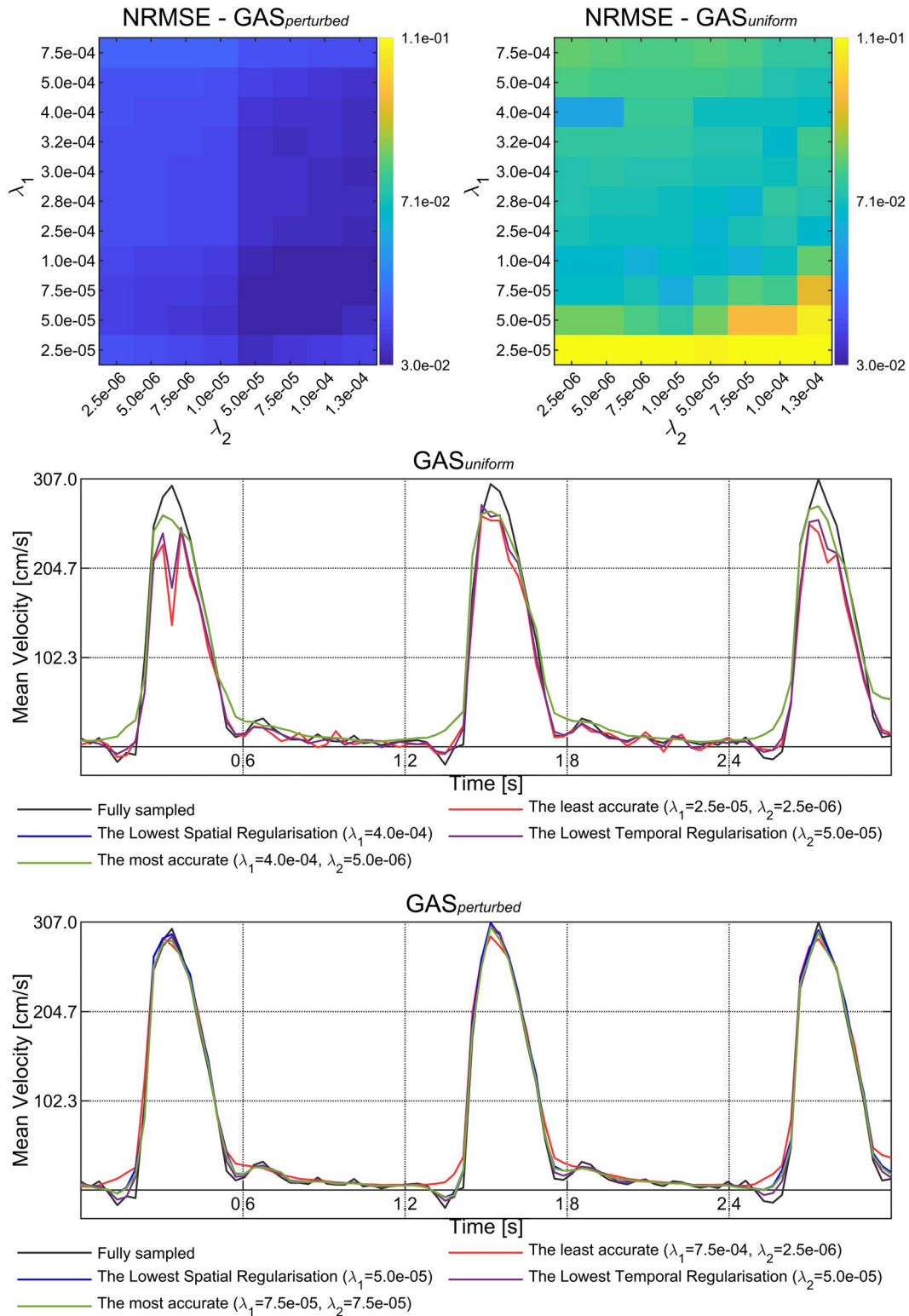
**FIGURE 5** In silico regularization-level optimization. The NRMSE results for GAS$_{perturbed}$ (top left) and GAS$_{uniform}$ (top right) are presented. The effects of regularization are shown with plots of 4 flow curves: the least accurate, the flow curve produced with the combination of regularization parameters that resulted in the worst NRMSE; the lowest spatial regularization ($\lambda_2 = 0.25e^{-5}$), the best result while varying only the temporal regularization ($\lambda_1$); the lowest temporal regularization ($\lambda_1 = 2.5e^{-5}$), the best result while varying only the spatial regularization ($\lambda_2$); and the most accurate, the combination of regularization parameters that produced the best NRMSE result. These were plotted against the flow curve extracted from the fully sampled spiral trajectory
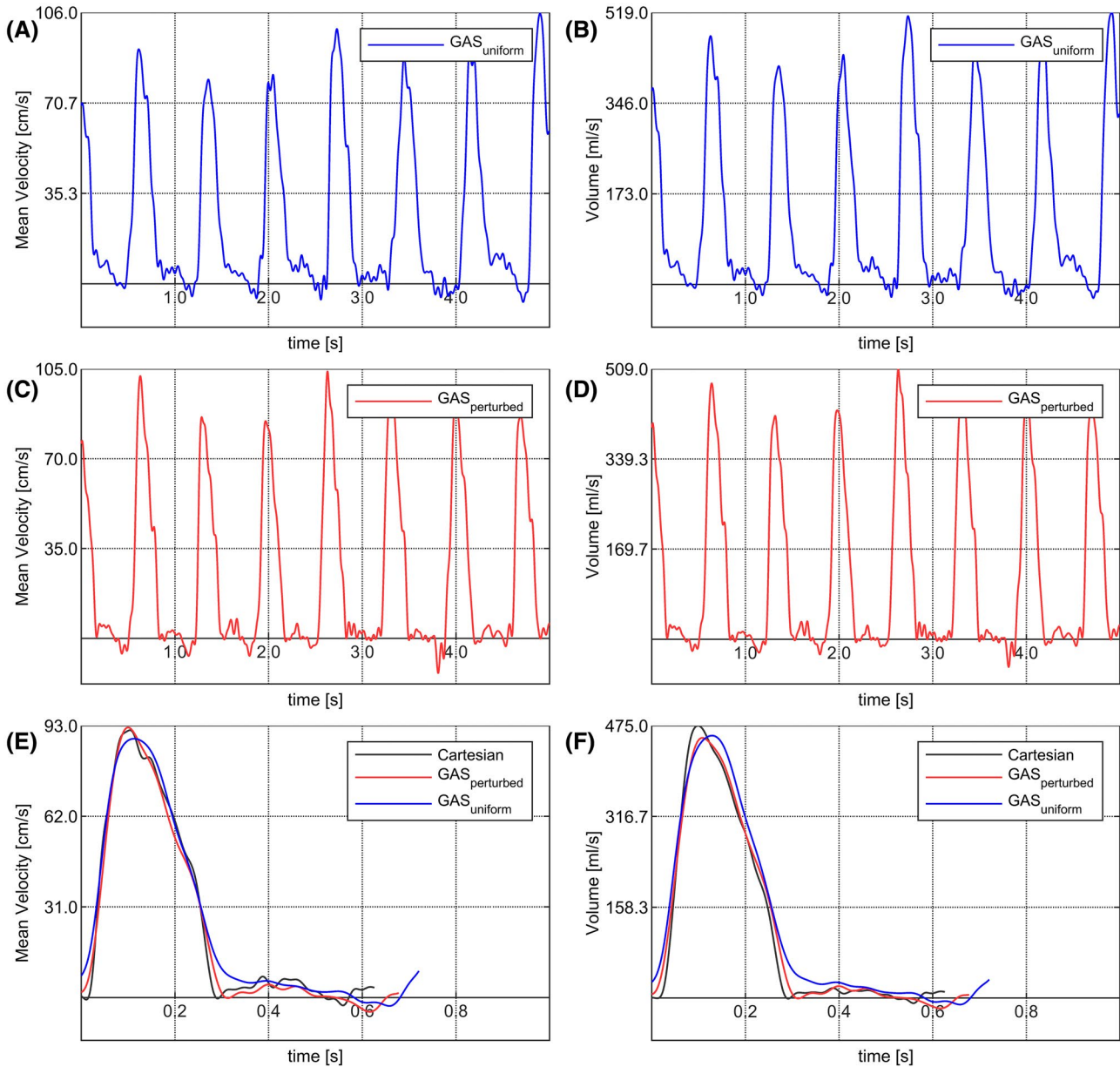
**FIGURE 6** Examples of flow and velocity curves from a single in vivo study subject. The mean velocity curves are shown in the left column (A,C,E) and the volume curves in the right column (B,D,F). The GAS$_{uniform}$ results are shown in the top row (A,B) against the GAS$_{perturbed}$ results in the middle row (C,D). For easier visual presentation, the individual r-r curves were interpolated into an average r-r curve. As electrocardiographic trigger points were not available, the r-r interval selection was done manually. The interpolated average curves were plotted against the reference curve from the Cartesian-gated acquisition in the bottom row (E,F)

acquisition produced a small insignificant underestimation of −1.8 mL (limits of agreement: −9.4 to 5.8 mL), whereas the GAS$_{uniform}$ acquisition produced a small, insignificant overestimation of 1.3 mL (limits of agreement: −8.8 to 11.4 mL).

## 3.5 | In vivo image quality

Representative imaging results are shown in Figure 8 and Supporting Information Videos S2-S4. No significant difference ($P = .28$) was found in the subjective image scoring between GAS$_{perturbed}$ (3.5 ± 0.6) and GAS$_{uniform}$ (3.3 ± 0.7) real-time imaging.

There was no significant difference ($P = .09$) in SNR between GAS$_{perturbed}$ (52.7 ± 25.8) and GAS$_{uniform}$ (36.6 ± 17.2) trajectories. However, both were substantially lower ($P < 0.001$) than Cartesian SNR (110.3 ± 38.6).

The VNR results showed no significant difference ($P = 0.99$) between Cartesian (16.1 ± 7.6) and GAS$_{perturbed}$ (16.3 ± 5.8) images, with both having significantly ($P < .02$) higher VNR than GAS$_{uniform}$ (12.1 ± 4.1) trajectory.
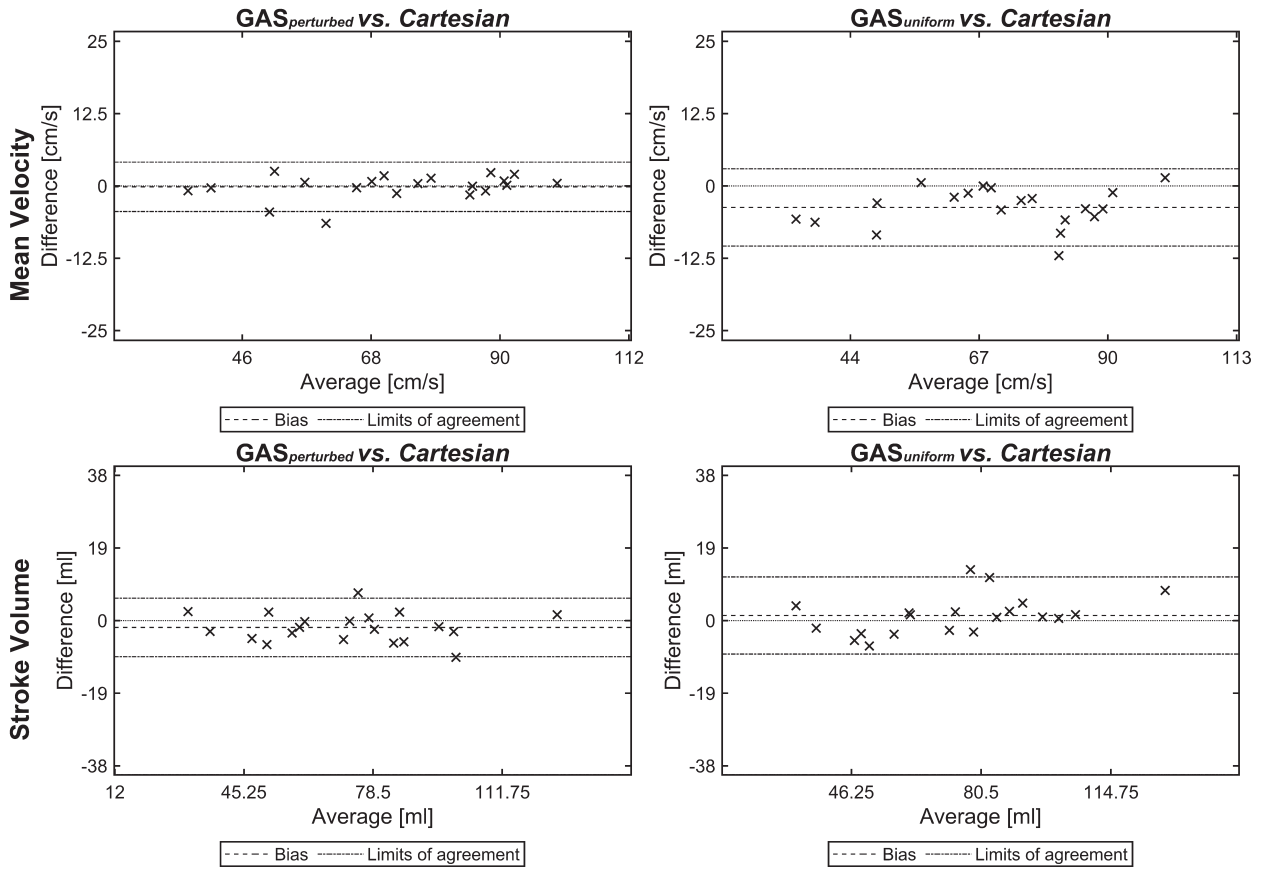
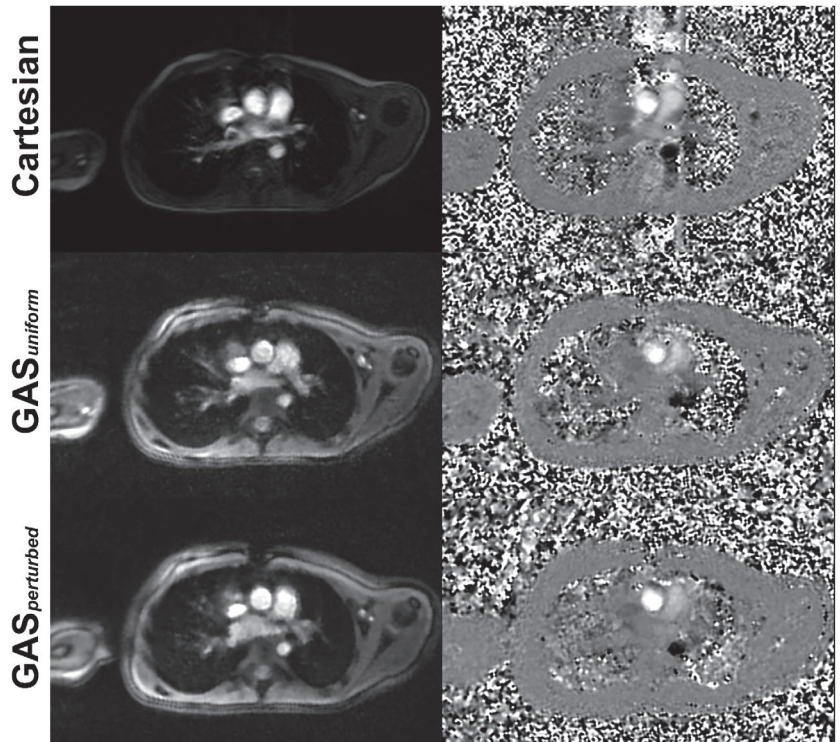**FIGURE 7** Stroke volume and peak mean velocity Bland-Altman plots



**FIGURE 8** Example of the in vivo imaging results

The average edge sharpness measure trended ($P = 0.14$) toward being higher in the Cartesian acquisition ($0.136 \pm 0.033$ mm$^{-1}$) compared with GAS$_{perturbed}$ ($0.119 \pm 0.037$ mm$^{-1}$) images. However, the Cartesian images were significantly ($P = .003$) sharper than GAS$_{uniform}$ ($0.105 \pm 0.034$ mm$^{-1}$) images. There was no statistically significant difference between the 2 GAS real-time acquisitions ($P = .27$).

# 4 | DISCUSSION

The main findings of the study were as follows: (1) CS reconstruction applied directly to GAS$_{uniform}$ PCMR data results in clinically significant blurring of velocity data; (2) the proposed GAS$_{perturbed}$ trajectory produces better conditioned data for CS reconstruction, as indicated with lower PSF energy leakage; and (3) this resulted in more accurate measurement of peak aortic velocity in silico and in vivo.

The benefit of combining CS with parallel imaging is that it allows much higher acceleration factors compared with parallel imaging alone (i.e., SENSE[5]) or temporal encoding (i.e., UNFOLD[9] or k-t BLAST[4]). However, the performance of CS is dependent on how well the algorithm's requirements are met, with the most difficult being incoherent aliasing. This is because most MR systems cannot produce the sharp, nonsmooth changes in gradient moments needed for true random sampling. Several studies have been undertaken to identify MR data sampling patterns that are conducive to CS.[17,32-38] It should be noted that gradient waveform design optimization for more complex trajectories has been done. However, these can be time-consuming algorithms with runtimes measured in minutes.[39]

A commonly taken approach is to combine non-Cartesian sampling with golden-angle rotations. Examples include both radial[11] and spiral[12] golden-angle acquisitions that use temporal total variation L1 regularization to remove imaging artifacts without introducing clinically important temporal blurring. However, real-time PCMR is a more challenging problem, as it requires higher acceleration factors (18 times in this study) due to the need for velocity-encoded and compensated readouts. In this study, we have shown that phase data are more susceptible to temporal regularization and that application of CS reconstruction to GAS$_{uniform}$ data resulted in significant blurring of velocity curves.

One possible solution is to perturb spiral trajectories to generate more incoherent artifacts, as suggested by Lustig et al.[40,41] However, to our knowledge, this approach has not been applied in clinical studies. This may be because in most applications adequate data quality can be obtained using more conventional methods. This is not the case for real-time PCMR; therefore, we designed a family of perturbed spiral trajectories that could be implemented on a standard clinical scanner. Using PSF energy leakage, we showed that spirals that were oversampled at the center with a low frequency oscillation in radial acceleration that slowly increased in amplitude had the greatest incoherence. When this GAS$_{perturbed}$ sampling pattern was tested in silico, it was demonstrated to be better conditioned for CS reconstruction than GAS$_{uniform}$. In particular, a high level of temporal regularization was required to remove coherent aliasing artifacts in GAS$_{uniform}$ data, resulting in significant temporal blurring. On the other hand, GAS$_{perturbed}$ data did not exhibit coherent aliasing artefacts, even at low levels of regularization. In addition, the greater spatial incoherence of the GAS$_{perturbed}$ aliases enabled spatial regularization to be used to further improve the image quality.

In the clinical study, both the GAS$_{perturbed}$ and GAS$_{uniform}$ acquisitions produced good-quality magnitude images with little residual artifacts. This is in keeping with previous studies that combined spiral imaging with CS reconstruction[12] and should be expected, as regularization was optimized for image quality. However, velocity and flow curves extracted from GAS$_{uniform}$ data were blurred in time compared with the reference standard Cartesian-gated data. This did not affect the quantification of stroke volume, as temporal blurring has a minimal effect on the integral of the flow curve. Nevertheless, it did result in significant underestimation of the peak mean velocities, which limits the clinical utility of GAS$_{uniform}$ real-time PCMR. In contrast, the GAS$_{perturbed}$ acquisition produced significantly less blurred flow and velocity curves. This resulted in good agreement with the Cartesian reference for both stroke volume and peak velocity quantifications. We believe that this demonstrates that the greater incoherence provided by perturbed spiral trajectories allows more accurate reconstruction of real-time PCMR data. This in turn widens the clinical utility of this technique in children with heart disease.

One well-recognized problem with spiral imaging is reduction in image quality due to trajectory errors. This can be mitigated by keeping readout lengths short and optimizing sampling bandwidth per pixel, as done in this study. There are also spiral deblurring algorithms available, although they were not used in this study as they would increase reconstruction time. A concern with perturbed spirals is that they might result in even greater trajectory errors. However, we saw no difference in qualitative image scores or edge sharpness between GAS$_{perturbed}$ and GAS$_{uniform}$ data. This suggests that trajectory errors were not seriously exacerbated by perturbing the spiral trajectory. Nevertheless, edge sharpness was slightly lower in the spiral acquisitions compared with the Cartesian data. This might be due to trajectory errors, the effect of spatial regularization, and the slightly lower acquired spatial resolution of the spiral acquisitions.

Another problem with spiral real-time approach is the lower SNR compared with the reference standard Cartesian acquisition. This is to be expected due to heavy undersampling of the real-time data and use of 2 signal averages for the Cartesian data. However, this does not appear to affect

subjective image quality. Interestingly, the VNR was lower in the GAS$_{uniform}$ data compared with both the Cartesian and GAS$_{perturbed}$ data. This can be attributed to the lower peak velocity in the GAS$_{uniform}$ data due to temporal blurring, rather than differences in the velocity SD.

A disadvantage of CS reconstructions is their complexity, translating into longer reconstruction times. This can become a bottleneck in the scanning protocol and consequently limits the clinical uptake. In this work, CS reconstruction was implemented using our in-house online graphics processing unit–based method.[18] This enabled clinically acceptable reconstruction times of 2 minutes 39 seconds for 270 images—the equivalent of about 7.2 seconds of scanning time. Further improvements could be achieved with adoption of faster reconstruction algorithms (i.e., ADMM[42]).

The described trajectory generation does not provide a simple sample density function. Furthermore, it is possible for readout paths to cross, which in some density calculations can lead to abnormal results (e.g., infinity, values smaller or equal to zero). To overcome this problem, we used the solution described by Bydder et al.[21] This algorithm takes a set of trajectory samples and returns optimal density compensation weights both flexibly and rapidly. However, this could be substituted with other more preferable sample density calculation algorithms if desired.

We recognize that the adopted golden-angle rotation between readouts dictates a fixed ordering of trajectory spiral arms. This, combined with a finite number of trajectory perturbations, restricts the range of possible trajectory variations. Relaxation of this condition could result in more incoherent sampling. However, this would substantially increase the computational cost of the optimal perturbation search process.

An additional difficulty lies in the selection of optimal regularization parameters. These can vary between studies and subjects. In this work, we used a composite L1 regularization (2D spatial and temporal total variation). A range of regularization parameters were tested for the in silico tests, and the parameters giving the lowest NRMSE were selected. In the in vivo study, no reference data were available, so we used an image quality–based optimization process in a single case. The parameters were then fixed for the whole study, but ideally this optimization process would be repeated for each patient. Unfortunately, this would be very time-consuming and not be feasible in the clinical environment. A solution might be the data-driven auto-tuning presented in the sparsity adaptive composite recovery algorithm.[43]

## 5 | CONCLUSIONS

We have validated a novel perturbed spiral PCMR acquisition for CS reconstruction. The work presents a significant improvement in spatio-temporal resolution of real-time PCMR data for cardiac MRI. The technique proved to be suitable for clinical use with the benefits of short acquisition times and no breathing artifacts. We believe the new technique has the potential to be a valuable tool in cardiovascular assessments, particularly in those patients for whom breath-holding is difficult.

## ORCID

*Grzegorz Tomasz Kowalik* https://orcid.org/0000-0003-3267-8652
*Jennifer Anne Steeden* https://orcid.org/0000-0002-9792-2022

## REFERENCES

1. Firmin DN, Nayler GL, Klipstein RH, Underwood SR, Rees RS, Longmore DB. In vivo validation of MR velocity imaging. *J Comput Assist Tomogr*. 1987;11:751–756.
2. Van Rossum AC, Sprenger M, Visser FC, Peels KH, Valk J, Roos JP. An in vivo validation of quantitative blood flow imaging in arteries and veins using magnetic resonance phase-shift techniques. *Eur Heart. J*. 1991;12:117–126.
3. Steeden JA, Atkinson D, Hansen MS, Taylor AM, Muthurangu V. Rapid flow assessment of congenital heart disease with high-spatiotemporal-resolution gated spiral phase-contrast MR imaging. *Radiology*. 2011;260:79–87.
4. Tsao J, Boesiger P, Pruessmann KP. k-t BLAST and k-t SENSE: dynamic MRI with high frame rate exploiting spatiotemporal correlations. *Magn Reson Med*. 2003;50:1031–1042.
5. Pruessmann KP, Weiger M, Scheidegger MB, Boesiger P. SENSE: sensitivity encoding for fast MRI. *Magn Reson Med*. 1999; 42:952–962.
6. Griswold MA, Jakob PM, Heidemann RM, et al. Generalized autocalibrating partially parallel acquisitions (GRAPPA). *Magn Reson Med*. 2002;47(6):1202–1210.
7. Kowalik GT, Steeden JA, Pandya B, et al. Real-time flow with fast GPU reconstruction for continuous assessment of cardiac output. *J Magn Reson Imaging*. 2012;36(6):1477–1482.
8. Beerbaum P, Korperich H, Gieseke J, Barth P, Peuster M, Meyer H. Rapid left-to-right shunt quantification in children by phase-contrast magnetic resonance imaging combined with sensitivity encoding (SENSE). *Circulation*. 2003;108(11):1355–1361.
9. Madore B, Glover GH, Pelc NJ. Unaliasing by fourier-encoding the overlaps using the temporal dimension (UNFOLD), applied to cardiac imaging and fMRI. *Magn Reson Med*. 1999;42:813–828.
10. Lustig M, Donoho D, Pauly JM. Sparse MRI: the application of compressed sensing for rapid MR imaging. *Magn Reson Med*. 2007;58:1182–1195.
11. Feng LI, Grimm R, Block KT, et al. Golden-angle radial sparse parallel MRI: combination of compressed sensing, parallel imaging, and golden-angle radial sampling for fast and flexible dynamic volumetric MRI. *Magn Reson Med*. 2014;72:707–717.
12. Steeden JA, Kowalik GT, Tann O, Hughes M, Mortensen KH, Muthurangu V. Real-time assessment of right and left ventricular volumes and function in children using high spatiotemporal resolution spiral bSSFP with compressed sensing. *J Cardiovasc Magn Reson*. 2018;20:79.

13. Kowalik G, Courot A, Steeden JA, Muthurangu V. Golden-angle spiral sparse parallel phase-contrast MR acquisition with an on-line fast GPU based reconstruction for high resolution real-time cardio-vascular assessments. In: Proceedings of the 25th Annual Meeting of ISMRM, Honolulu, Hawaii, 2017. Abstract #1262.

14. Pipe JG, Zwart NR. Spiral trajectory design: a flexible numerical algorithm and base analytical equations. *Magn Reson Med*. 2014;71:278–285.

15. Lauzon ML, Rutt BK. Polar sampling in k-space: reconstruction effects. *Magn Reson Med*. 1998;40:769–782.

16. Lauzon ML, Rutt BK. Effects of polar sampling in k-space. *Magn Reson Med*. 1996;36:940–949.

17. Ahmad R, Potter L, Kuppusamy P. Oscillating radial trajectories for reduced undersampling artifacts. In: Proceedings of the 17th Annual Meeting of ISMRM, Honolulu, Hawaii, 2009:575.

18. Kowalik GT, Steeden JA, Muthurangu V. Implementation of a generalized heterogeneous image reconstruction system for clinical magnetic resonance. *Concurr Comput Pract E*. 2015; 27:1603–1611.

19. O'Sullivan JD. A fast sinc function gridding algorithm for fourier inversion in computer tomography. *IEEE Trans Med Imaging*. 1985;4:200–207.

20. Jackson JI, Meyer CH, Nishimura DG, Macovski A. Selection of a convolution function for Fourier inversion using gridding [computerised tomography application]. *IEEE Trans Med Imaging*. 1991;10:473–478.

21. Bydder M, Samsonov AA, Du J. Evaluation of optimal density weighting for regridding. *Magn Reson Imaging*. 2007;25: 695–702.

22. Pruessmann KP, Weiger M, Bornert P, Boesiger P. Advances in sensitivity encoding with arbitrary k-space trajectories. *Magn Reson Med*. 2001;46:638–651.

23. Odille F, Steeden JA, Muthurangu V, Atkinson D. Automatic segmentation propagation of the aorta in real-time phase contrast MRI using nonrigid registration. *J Magn Reson Imaging*. 2011;33:232–238.

24. Rosset A, Spadola L, Ratib O. OsiriX: an open-source software for navigating in multidimensional DICOM images. *J Digit Imaging*. 2004;17:205–216.

25. Dietrich O, Raya JG, Reeder SB, Reiser MF, Schoenberg SO. Measurement of signal-to-noise ratios in MR images: influence of multichannel coils, parallel imaging, and reconstruction filters. *J Magn Reson Imaging*. 2007;26:375–385.

26. Muthurangu V, Lurz P, Critchely JD, Deanfield JE, Taylor AM, Hansen MS. Real-time assessment of right and left ventricular volumes and function in patients with congenital heart disease by using high spatiotemporal resolution radial k-t SENSE. *Radiology*. 2008;248:782–791.

27. Steeden JA, Atkinson D, Taylor AM, Muthurangu V. Split-acquisition real-time CINE phase-contrast MR flow measurements. *Magn Reson Med*. 2010;64:1664–1670.

28. Duchon CE. Lanczos filtering in one and two dimensions. *J Appl Meteorol*. 1979;18:1016–1022.

29. Turkowski K. *Filters for common resampling tasks. Graphics Gems*. San Diego, CA: Academic Press Professional; 1990:147–165.

30. Holoborodko P. Smooth noise robust differentiators. 2008. http://www.holoborodko.com/pavel/numerical-methods/numerical-derivative/smooth-low-noise-differentiators/. Accessed October 31, 2019.

31. Meek G, Ozgur C, Dunning K. Comparison of the t vs. Wilcoxon signed-rank test for Likert scale data and small samples. *JMASM*. 2007;6:91–106.

32. Lustig M, Pauly JM. SPIRiT: iterative self-consistent parallel imaging reconstruction from arbitrary k-space. *Magn Reson Med*. 2010;64:457–471.

33. Knoll F, Clason C, Diwoky C, Stollberger R. Adapted random sampling patterns for accelerated MRI. *MAGMA*. 2011;24:43–50.

34. Li Y, Yang R, Zhang C, Zhang J, Jia S, Zhou Z. Analysis of generalized rosette trajectory for compressed sensing MRI. *Med Phys*. 2015;42:5530–5544.

35. Ahmad R, Xue H, Giri S, Ding Y, Craft J, Simonetti OP. Variable density incoherent spatiotemporal acquisition (VISTA) for highly accelerated cardiac MRI. *Magn Reson Med*. 2015;74:1266–1278.

36. Li Y, Yang R, Zhang ZP, Wu YX. Chaotic-like k-space trajectory for compressed sensing MRI. *J Med Imaging Health Inform*. 2015;5:415–421.

37. Yang Y, Kramer CM, Shaw PW, Meyer CH, Salerno M. First-pass myocardial perfusion imaging with whole-heart coverage using L1-SPIRiT accelerated variable density spiral trajectories. *Magn Reson Med*. 2016;76:1375–1387.

38. Lazarus C, Weiss P, Chauffert N, et al. SPARKLING: variable-density k-space filling curves for accelerated T2(*)-weighted MRI. *Magn Reson Med*. 2019;81:3643–3661.

39. Chauffert N, Weiss P, Kahn J, Ciuciu P. A projection algorithm for gradient waveforms design in magnetic resonance imaging. *IEEE Trans Med Imaging*. 2016;35:2026–2039.

40. Lustig M, Lee JH, Donoho DL, Pauly JM. Faster imaging with randomly perturbed, under-sampled spirals and l1 reconstruction. In: Proceedings of the 13th Annual Meeting of ISMRM, Miami Beach, Florida, 2005:685.

41. Lustig M, Kim SJ, Pauly JM. A fast method for designing time-optimal gradient waveforms for arbitrary k-space trajectories. *IEEE Trans Med Imaging*. 2008;27:866–873.

42. Wang Y, Ying L. Compressed sensing dynamic cardiac cine MRI using learned spatiotemporal dictionary. *IEEE Trans Biomed Eng*. 2014;61:1109–1120.

43. Chen C, Liu Y, Schniter P, et al. Sparsity adaptive reconstruction for highly accelerated cardiac MRI. *Magn Reson Med*. 2019; 81:3875–3887.

## SUPPORTING INFORMATION

Additional supporting information may be found online in the Supporting Information section.

**FIGURE S1** Visual representation of Equy 1. The plots were done for 3 sets of parameters, including the optimized $GAS_{perturbed}$. The plots show a ramped increase in radial acceleration (from $c_0$ to $c_1$). From the k-space center to $c_0$, the acceleration is constant ($\alpha_r = 0.5$ - oversampling). From $c_0$ to $c_1$, the maximum acceleration increases linearly from 0.5 to $\alpha_0 = 0.5$, where it stabilizes. Also, starting from $c_0$, the sinusoidal oscillations are imposed onto the radial acceleration. The value of $\phi_0$ does not vary with progression of a trajectory through k-space. It is a constant based on a starting angle of a trajectory readout from the k-space center. The left plots

show radial acceleration ($\alpha_r$) variations for 3 readouts. These come out of the k-space center in 3 evenly distributed directions: $\phi_0 = \left\{ 0, \frac{2\pi}{3}, \frac{4\pi}{3} \right\}$

**FIGURE S2** Trajectory visualization. Shown are the GAS$_{\text{uniform}}$, GAS$_{\text{perturbed}}$, and an additional example presenting possible perturbations induced to the spiral trajectory. The $k_x$-$k_y$ positions of composite trajectories are presented for 3 consecutive imaging frames. Additionally, variations in the coordinates ($k_x$ and $k_y$) are plotted against time

**FIGURE S3** In silico phantom. The model consisted of a big ellipse representing a chest cross section. Additional 3 internal ellipses were used to portray ascending aorta, descending aorta, and pulmonary arch. The outer ellipse was surrounded with a high-intensity border representing subcutaneous fat. Internal cavities were inserted to represent lungs. The upper part of the figure presents imaging results of the SENSE-reconstructed in silico data generated on a uniform density spiral trajectory. The bottom plots show temporal changes in phase (flow data), size of the body, as well as size and position of the aorta

**FIGURE S4** Comparison of PSFs. A, The PSFs of the initial trajectory (GAS$_{\text{uniform}}$). B, The PSFs of the final selected GAS$_{\text{perturbed}}$ trajectory. C, The PSFs for an example of perturbed trajectory. Multiple of rings that do not change their spatial location can be observed in the PSF of GAS$_{\text{uniform}}$ (A). A broader spatial distribution of the aliasing rings can be observed on the PSFs of the perturbed trajectories

**VIDEO S1** Normalized PSFs of GAS$_{\text{uniform}}$ and GAS$_{\text{perturbed}}$ plotted using logarithmic scale

**VIDEO S2** Magnitude and phase of the Cartesian-gated phase-contrast magnetic resonance (PCMR) reconstruction for the example presented in Figure 7

**VIDEO S3** Magnitude and phase of the GAS$_{\text{uniform}}$ real-time PCMR reconstruction for the example presented in Figure 7

**VIDEO S4** Magnitude and phase of the GAS$_{\text{perturbed}}$ real-time PCMR reconstruction for the example presented in Figure 7